J Nanopart Res (2014) 16:2328
DOI 10.1007/s11051-014-2328-z

RESEARCH PAPER

Influence of low-energy plasma annealing on structural and optical properties of silver nanoclusters grown by magnetron sputtering deposition

V. Antad · L. Simonot · D. Babonneau

Received: 18 July 2013 / Accepted: 11 February 2014 / Published online: 22 February 2014

Abstract Structural and optical modifications induced by low-energy (≤80 eV) bias-plasma annealing of silver nanoclusters (2–25 nm) grown by magnetron sputtering deposition are reported. By combining postmortem structural characterizations and real-time optical measurements, we show that etching effects associated with enhanced Ag mobility result in progressive and irreversible changes of both the morphology and organization of the nanoclusters (i.e., decrease of the cluster size and intercluster distance as well as increase of their out-of-plane aspect ratio). Surface plasmon resonance bands of the nanoclusters are also modified by plasma treatment, which causes a blue-shift together with an amplitude decrease and a narrowing of the band. In addition, the kinetics of plasma-induced modifications can be easily controlled by varying the applied bias voltage. Therefore, plasma annealing could emerge as an efficient alternative to more traditional thermal annealing treatments for tuning the plasmonic properties of noble metal nanoclusters with great flexibility.

Keywords Magnetron sputtering · Silver nanoparticles · Surface plasmon resonance · Plasma annealing · Surface differential reflectance spectroscopy

V. Antad · L. Simonot (✉) · D. Babonneau
Départment Physique et Mécanique des Matériaux, Institut Pprime, UPR 3346 CNRS, Université de Poitiers, SP2MI, 11 Bvd M. & P. Curie, BP 30179, 86962 Futuroscope Chasseneuil Cedex, France
e-mail: lionel.simonot@univ-poitiers.fr

Present Address:
V. Antad
Department of Physics, University of Pune, Ganeshkhind, Pune 411007, India

Introduction

In contrast to their bulk form, nanosized metals surrounded by a dielectric medium exhibit a remarkable optical phenomenon known as localized surface plasmon resonance (SPR) when they interact with visible light (Kreibig and Vollmer 1995). Excitation of surface plasmons in metal nanoclusters at the resonance wavelength results in an intense optical absorption and a strong enhancement of the local field around the nanoclusters. Such particular properties are the bases of recent significant developments, which exploit "engineered" metal nanoclusters for various applications ranging from photonic and photovoltaic devices to biochemical sensors and markers (Maier and Atwater 2005; Polman 2008; Schuller et al. 2010; Ren et al. 2011). The spectral position, amplitude, and width of the SPR bands are highly sensitive to the size, shape, organization, and type of the metal nanoclusters as well as to their surrounding environment (Mock

et al. 2002; Toudert et al. 2005; Kinnan and Chumanov 2010). Furthermore, due to their large surface to volume ratio, metal nanoclusters are strongly sensitive to post-fabrication (physical or chemical) treatments such as thermal annealing (TA) (Teranishi et al. 2001; Kolmakov and Goodman 2002; Pan et al. 2003; Takele et al. 2008) or exposure to controlled atmospheres (Iline et al. 1999; Bi et al. 2002; Serna et al. 2002; Hu et al. 2005; Borensztein et al. 2010; Antad et al. 2012). In this way, structural and chemical properties of metal nanoclusters can be tailored, and their associated SPR characteristics can be optimized for specific applications.

Among physical routes, TA is commonly used to modify the structural and optical properties of noble metal nanoclusters. In most cases, supported nanoclusters grown on dielectric surfaces by physical vapor deposition do not reach their equilibrium shape expressed by the Wulff–Kaischew theorem (Henry 2005). By heating such supported nanoclusters at appropriate temperatures for sufficient durations, atomic or cluster migration is usually promoted, which results in cluster growth by coalescence (i.e., increase of the cluster size and intercluster distance), change of the cluster shape (i.e., increase of the out-of-plane aspect ratio), and gives rise to narrower size and shape distributions. Structural modifications generated by heating induce changes of the SPR characteristics accordingly, i.e., the spectral position of the SPR is seen to blue-shift after TA, whereas its amplitude increases and its width narrows. However, it should be noted that use of high temperatures (>150 °C) can be inadequate for post-fabrication treatments of nanoclusters deposited on some substrates, such as flexible and transparent polymers.

It has recently been shown that the morphology and/or the plasmonic response of supported nanoclusters can also be modified by surrounding them with a low-temperature plasma (Tang et al. 2011; Lapsley et al. 2012; Bedel et al. 2012; Antad et al. 2013). For example, Lapsley et al. (2012) have demonstrated that charge-induced plasmonic shifts can be generated using argon plasma to charge arrays of Au nanodisks. On the other hand, Bedel et al. (2012) have evidenced significant changes in the average size and organization of Ag nanoclusters subjected to a plasma during their encapsulation by a SiO_xC_y layer. Moreover, Antad et al. (2013) have reported that plasma annealing (PA) at low energy (<50 eV) can also be used as a simple and effective method to restore the SPR of oxidized Ag nanoclusters. While PA thus opens up new opportunities for developing plasmon-based devices with high tunability of the SPR, the influence of the applied bias voltage and the cluster size of plasma-annealed noble metal nanoclusters has not been investigated in detail so far. In this article, based on high-angle annular dark-field scanning transmission electron microscopy (HAADF-STEM), grazing incidence small-angle X-ray scattering (GI-SAXS), and real-time surface differential reflectance spectroscopy (SDRS), PA-induced structural and optical modifications of non oxidized Ag nanoclusters grown by magnetron sputtering deposition are studied. Both the influence of the applied bias voltage (between 25 and 80 V) and the cluster size (between 2 and 25 nm) is examined and compared with changes produced by traditional TA. Our results show unambiguously that low-energy PA could be a potential alternative to TA for manipulating the nanostructures of noble metal nanoclusters with various sizes and their SPR characteristics with strong flexibility over large active areas.

Experimental details

Si_3N_4 (20 nm):Ag (t_{Ag}):Si_3N_4 (40 nm) nanocomposite thin films were grown at 200 °C onto glass substrates and carbon-coated copper grids in a custom vacuum chamber equipped with two magnetrons inclined at 25° from the substrate normal (Antad et al. 2012, 2013; Simonot et al. 2010), as shown in Fig. 1a. The first and final steps of the multi-stage growth process (Fig. 2) consisted in depositing amorphous Si_3N_4 layers by radiofrequency (RF) reactive sputtering at a rate of 0.03 nm/s. In the second step, Volmer–Weber growth of Ag was accomplished by direct current sputtering at a rate of 0.10 nm/s resulting in the formation of isolated Ag nanoclusters on the surface of the first Si_3N_4 (buffer) layer. With the aim of investigating the influence of the nanocluster size on plasma annealing effects, the effective thickness of deposited Ag was $t_{Ag} = 1$, 2, or 4 nm. After Ag deposition, no action was taken for 600 s to give the nanoclusters sufficient time to stabilize on the surface. Then, before capping them with a final Si_3N_4 layer, the nanoclusters were subjected to PA or TA treatments. For comparison, similar non-annealed

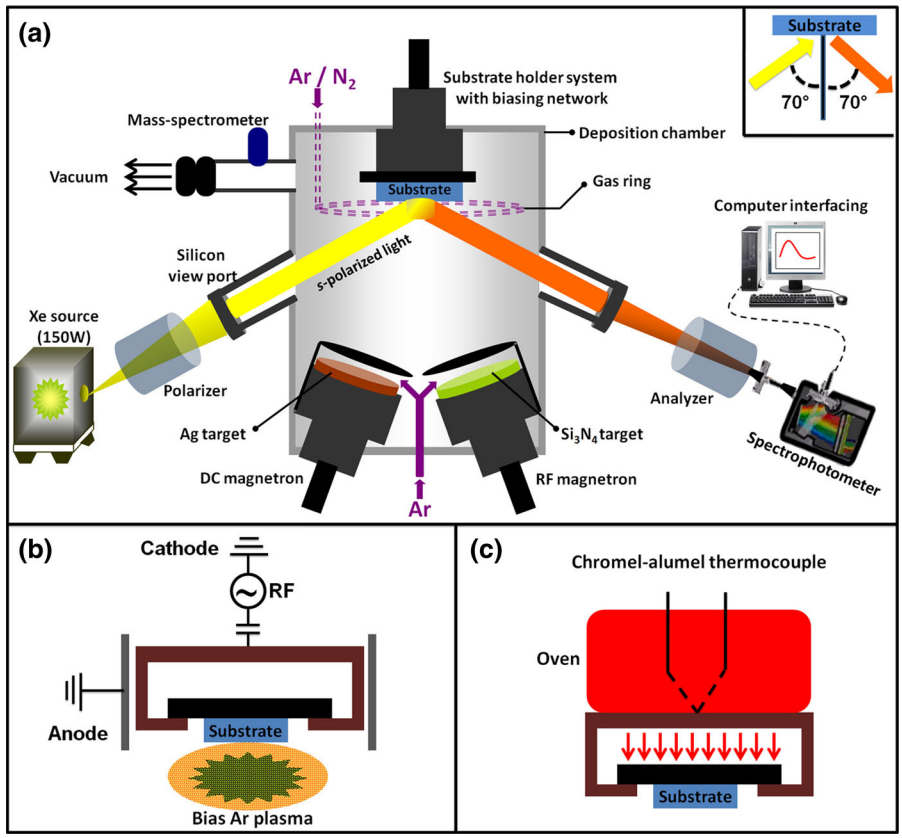

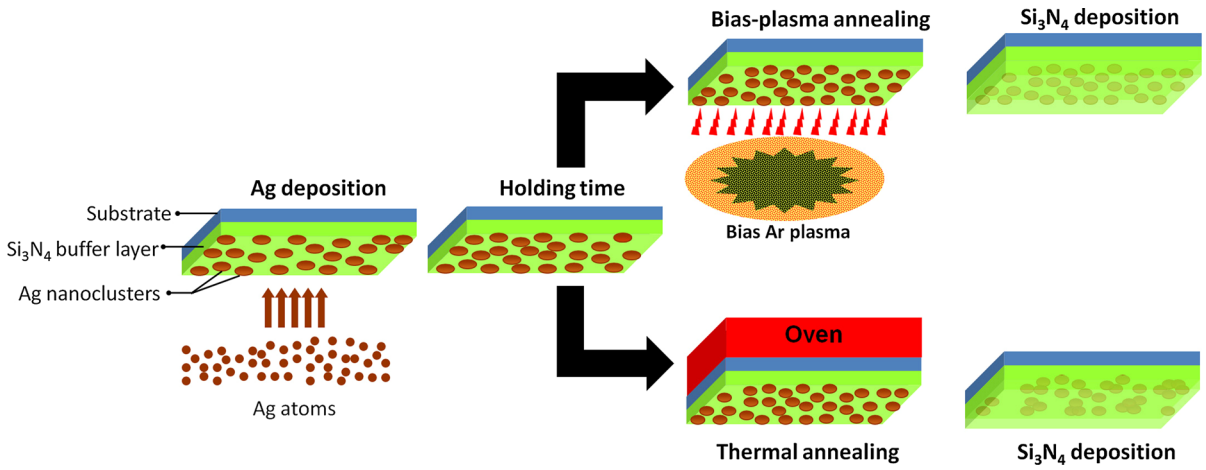

Fig. 1 Schematics of **a** magnetron sputtering system used to fabricate nanocomposite thin films along with in situ SDRS device for real-time optical monitoring, **b** plasma annealing system to create a controlled bias Ar plasma, **c** heating system to perform traditional thermal annealing

Fig. 2 Schematics of the multi-stage growth process employed to fabricate Si_3N_4:Ag (t_{Ag}):Si_3N_4 nanocomposite thin films with plasma annealing or thermal annealing treatments (see text for details)

(NA) nanocomposite thin films with corresponding effective Ag thicknesses, t_{Ag}, were also studied.

Assemblies of Ag nanoclusters with various sizes were treated by low-energy PA for 1,200 s after the creation of a controlled bias Ar plasma. Argon gas was introduced in the vicinity of the substrate holder at a flow rate of 6 sccm (corresponding to a partial pressure of 10^{-3} mbar) and was ionized by establishing a RF

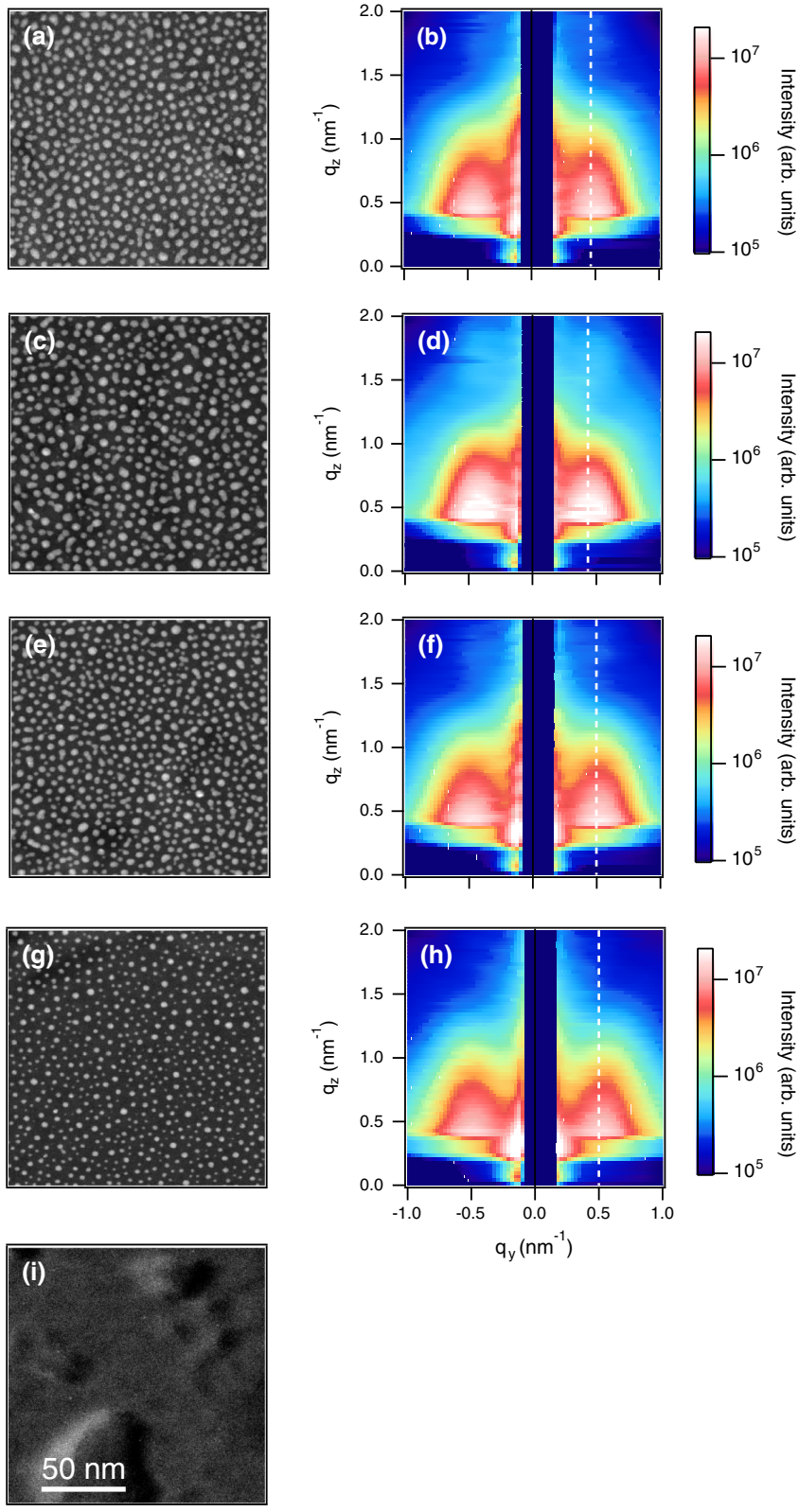

Fig. 3 Comparison of HAADF-STEM micrographs (1st column) and 2D experimental GISAXS patterns (2nd column) of Si_3N_4:Ag (2 nm):Si_3N_4 nanocomposite thin films subjected to different treatments during the multi-stage preparation process: **a**–**b** NA thin film, **c**–**d** TA-treated thin film, **e**–**f** PA-treated thin film at 25 eV, **g**–**h** PA-treated thin film at 50 eV, **i** PA-treated thin film at 80 eV. Dashed lines correspond to the q_y-position of the intensity maximum in the 2D GISAXS patterns

bias voltage (25, 50, or 80 V) between the substrate holder and the surrounding cylinder, as shown in Fig. 1b. Similarly, Ag nanoclusters were treated by traditional TA at 400 °C for 3,600 s with an in situ heating system placed 2 mm above the susbtrate holder, as shown in Fig. 1c. The temperature, measured using a chromel–alumel thermocouple, was increased from 200 to 400 °C at a rate of about 44 °C/min and was allowed to break down to 200 °C by natural cooling ($\sim$3 °C/min) after thermal treatment and before capping-layer deposition.

NA, PA-, and TA-treated Si_3N_4:Ag (t_{Ag}):Si_3N_4 nanocomposite thin films were characterized from in-plane views by HAADF-STEM with a JEOL 2200FS microscope using an acceleration voltage of 200 kV, a probe size of 0.7 nm, and an inner collection angle of 50 mrad. Quantitative information on the inter-cluster distance L, average in-plane diameter D of the nanoclusters, and associated standard deviation σ_D were determined by image processing techniques (Lantiat et al. 2007). In addition, GISAXS experiments were performed under vacuum at the D2AM beamline (European Synchrotron Radiation Facility, Grenoble). The focus of the incident X-ray beam on the sample was 0.4 mm (H) × 0.1 mm (V) (full width at half maximum), and the energy of 9.8 keV was selected to measure the samples with an incidence angle $\alpha_i \approx 0.25°$. The transmitted and specularly reflected beams were masked by a vertical beam-stop, and the scattered intensity was collected with a two-dimensional (2D) charge-coupled device (CCD) detector placed either at 715 mm or at 1,960 mm from the sample. The experimental data, corrected for the background and non-uniform sensitivity of the CCD, were analyzed within the distorted wave-Born approximation using the *FitGISAXS* program (Babonneau 2010) assuming polydisperse hemispheroidal Ag nanoclusters with in-plane diameter D and height H sandwiched between two Si_3N_4 layers (with thicknesses of 40 and 20 nm, respectively) deposited onto a semi-infinite glass substrate. The average in-plane diameter D value and the related dispersion σ_D were fixed to the values determined from HAADF-STEM. Least-squares fitting of 2D experimental data yielded the average height H of the nanoclusters.

Both ex situ (postmortem) and in situ (real-time) optical characterization techniques were employed to measure the optical response of the Si_3N_4:Ag (t_{Ag}):Si_3N_4 nanocomposite thin films. Ex situ reflectance measurements were carried out after the whole deposition/treatment process using a Varian Cary 5000 spectrophotometer at near-normal incidence (7°) in the 350–1,200 nm range. Furthermore, in situ SDRS was employed during both deposition steps and treatment steps using a home-made system installed in a non-intrusive way for real-time optical monitoring, as shown in Fig. 1a. The sample surface was illuminated using *s*-polarized light at an oblique incidence angle (70°) to study the SPR with an excitation in the plane of the sample. A discharge xenon lamp (150 W) was employed as a white light source, and the reflected intensity $R(\lambda,t)$ at time t was collected in the specular direction by a QE65000 spectrophotometer (Ocean Optics^{TM}) at a rate of one spectrum per second within the spectral range $\lambda = 350$–800 nm. The reflectance of the first Si_3N_4 layer, $R_0(\lambda) = R(\lambda,t = 0)$, was taken as a reference and, as soon as Ag deposition started, the SDRS signal was obtained from the differential change of the reflected intensity given by

$$\frac{\Delta R}{R_0}(\lambda, t) = \frac{R(\lambda, t) - R_0(\lambda)}{R_0(\lambda)} \quad (1)$$

Results and discussion

Influence of annealing treatments on the structural properties of Ag nanoclusters

Figure 3a displays a representative plan-view HAADF-STEM micrograph of a NA Si_3N_4:Ag (2 nm):Si_3N_4 nanocomposite thin film where the formation of a polydisperse assembly of isolated Ag nanoclusters (bright zones) embedded in an amorphous Si_3N_4 matrix (dark zones) is obvious. Such a structure gives rise to two distinct scattering lobes in the corresponding 2D GISAXS pattern (Fig. 3b). In comparison, a visual inspection of HAADF-STEM micrograph (Fig. 3c) and GISAXS pattern (Fig. 3d) of a TA-treated Si_3N_4:Ag (2 nm):Si_3N_4 nanocomposite thin film does not reveal a significant influence of the TA treatment on the morphology and organization of the Ag nanoclusters. However, from the quantitative analysis of the HAADF-STEM and GISAXS data gathered in Table 1, general conclusions can be drawn. As expected, NA nanocomposite thin films with increasing effective thicknesses of deposited Ag,

Table 1 Structural parameters and corresponding SPR position (λ_R) of non-annealed (NA) Ag nanoclusters compared with Ag nanoclusters subjected to thermal annealing (TA) and plasma annealing (PA) treatments

t_{Ag} (nm)	Treatment	L (nm)	D (nm)	σ_D (nm)	H (nm)	λ_R (nm)
1	NA	10.0	4.4	1.4	2.8	615
1	TA (400 °C)	11.0	4.3	1.5	2.8	600
1	PA (25 eV)	9.1	3.5	1.2	2.8	570
2	NA	12.6	7.6	1.9	4.4	645
2	TA (400 °C)	14.0	7.2	2.1	4.9	590
2	PA (25 eV)	11.9	6.3	1.6	4.6	575
2	PA (50 eV)	12.1	4.6	1.5	4.1	550
2	PA (80 eV)	–	–	–	–	–
4	NA	19.4	13.6	3.6	6.9	735
4	TA (400 °C)	21.5	13.2	4.2	7.3	680
4	PA (25 eV)	18.7	12.2	3.0	7.5	665

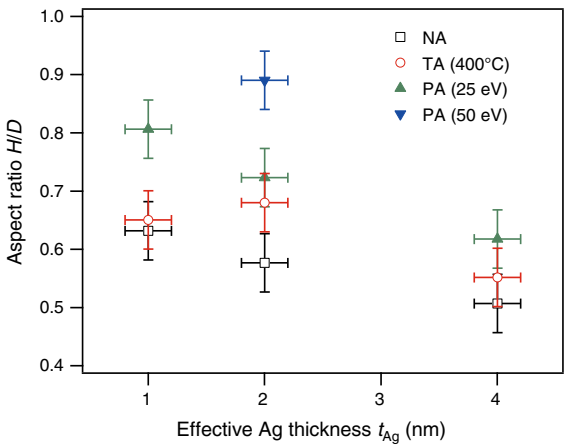

Fig. 4 Out-of-plane aspect ratios for Ag nanoclusters in Si_3N_4:Ag (t_{Ag}):Si_3N_4 nanocomposite thin films subjected to different treatments during the multi-stage preparation process: non-annealed (NA), thermally annealed at 400 °C (TA), and plasma annealed at 25 or 50 eV (PA)

t_{Ag}, display nanoclusters with larger sizes (D and H), dispersion (σ_D), and intercluster distances (L). As the rate of lateral growth is higher than the rate of vertical growth, smaller H/D ratios at higher t_{Ag} are witnessed, as shown in Fig. 4. Besides, whatever t_{Ag}, TA results in an increase of the intercluster distance L (i.e., decrease of the areal cluster density) together with a slight decrease of the average in-plane diameter D of the nanoclusters. Furthermore, TA induces an increase of the average height H of the nanoclusters and, accordingly, their out-of-plane aspect ratio H/D is enlarged in comparison with corresponding NA samples (Fig. 4). Overall, this behavior is in agreement with results reported in the literature (Teranishi et al. 2001; Takele et al. 2008; Dong et al. 2006; Ruffino et al. 2008; Pan et al. 2003; Heilmann and Werner 1998; Bhattacharyya et al. 2009) and can be ascribed to an enhanced Ag mobility during TA, thus promoting atomic or cluster migration and coalescence as well as reshaping processes.

In contrast with TA at 400 °C, PA causes structural modifications of the Ag nanoclusters, which are visible at a glance in Fig. 3e–i. Both the HAADF-STEM micrograph and GISAXS pattern of the nanocomposite thin film with $t_{Ag} = 2$ nm treated at 25 eV reveal a decrease of the in-plane cluster diameter D, and intercluster distance L. These effects appear to be more pronounced upon treatment at 50 eV, while no Ag clusters are detected in the HAADF-STEM micrograph of the nanocomposite thin film treated at 80 eV suggesting total Ag re-evaporation by etching. The structural parameters retrieved from the quantitative analysis of the HAADF-STEM and GISAXS data for various plasma-annealed Si_3N_4:Ag(t_{Ag}):Si_3N_4 nanocomposite thin films are reported in Table 1. Moreover, corresponding out-of-plane aspect ratios H/D and in-plane size distributions are compared with NA samples in Figs. 4 and 5, respectively. It can be observed that, in addition to the decrease of the in-plane cluster diameter and intercluster distance, PA treatment also induces a slight narrowing of the size distribution along with a significant increase of the out-of-plane ratio of the nanoclusters. Furthermore, the structural modifications are reproduced for all the nanocomposite thin films treated at 25 eV (with the influence of the PA

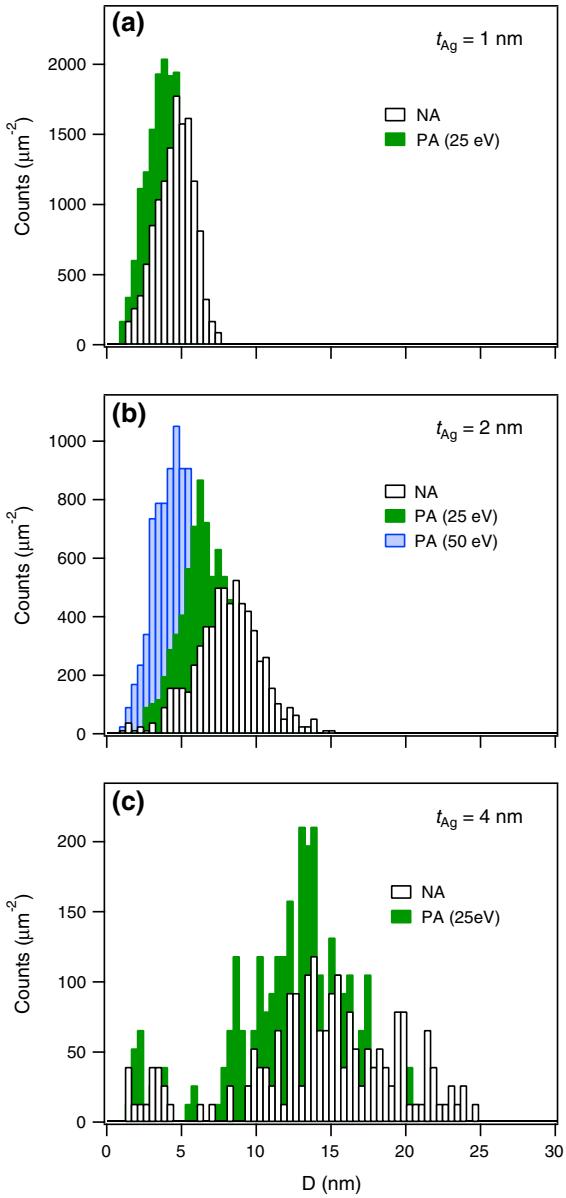

Fig. 5 In-plane size distributions for Ag nanoclusters in Si_3N_4:Ag (t_{Ag}):Si_3N_4 nanocomposite thin films subjected to PA at 25 or 50 eV during the multi-stage preparation process: **a** $t_{Ag} = 1$ nm, **b** $t_{Ag} = 2$ nm, and **c** $t_{Ag} = 4$ nm. In-plane size distributions for Ag nanoclusters in non-annealed Si_3N_4:Ag (t_{Ag}):Si_3N_4 nanocomposite thin films are also shown for comparison

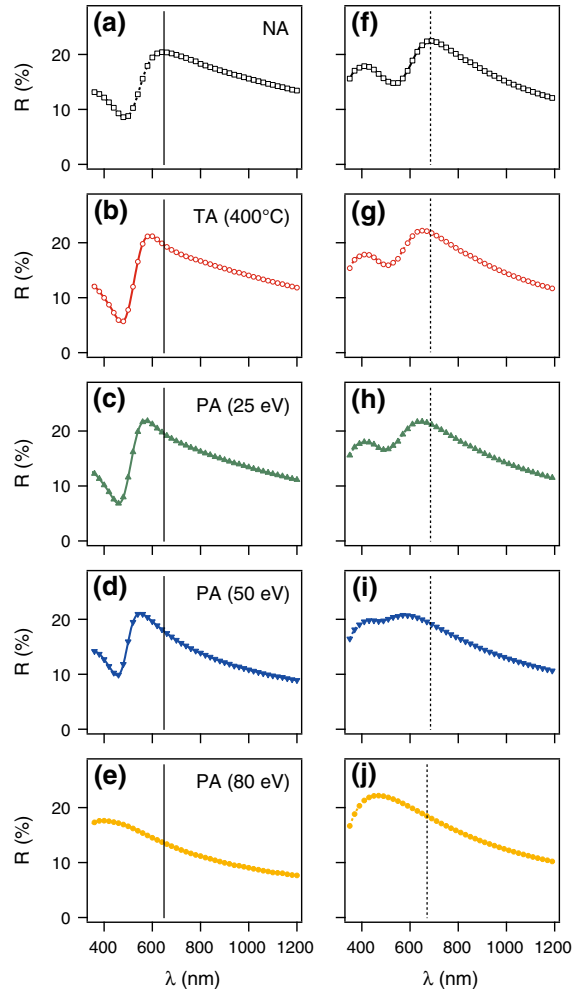

Fig. 6 **a**–**e** Experimental and **f**–**j** simulated reflectance spectra of Si_3N_4:Ag (2 nm):Si_3N_4 nanocomposite thin films: **a**, **f** non-annealed (NA), **b**, **g** thermally annealed at 400 °C (TA), and plasma annealed (PA) at **c**, **h** 25 eV, **d**, **i** 50 eV, and **e**, **j** 80 eV. *Vertical lines* correspond to the spectral position of the reflectance maximum for the NA sample ($\lambda_R \approx 645$ nm)

being more pronounced at smaller t_{Ag}) while reinforcing clearly for PA at 50 eV. In comparison with the TA treatment that causes a decrease of the areal cluster density, our results suggest the absence of coalescence-type growth processes during the PA of Ag nanoclusters. In the literature, it has been already reported that upon interactions with low-energy plasma, surface defects such as vacancies can be created on the substrate, which can act as pinpoints or nucleation sites for metal adatoms (Esch et al. 1995; Chey and Cahill 1997). This phenomenon associated with etching and re-deposition effects may explain the increase of the areal cluster density together with the decrease of the in-plane cluster diameter upon plasma annealing. These results convincingly demonstrate that PA treatments can

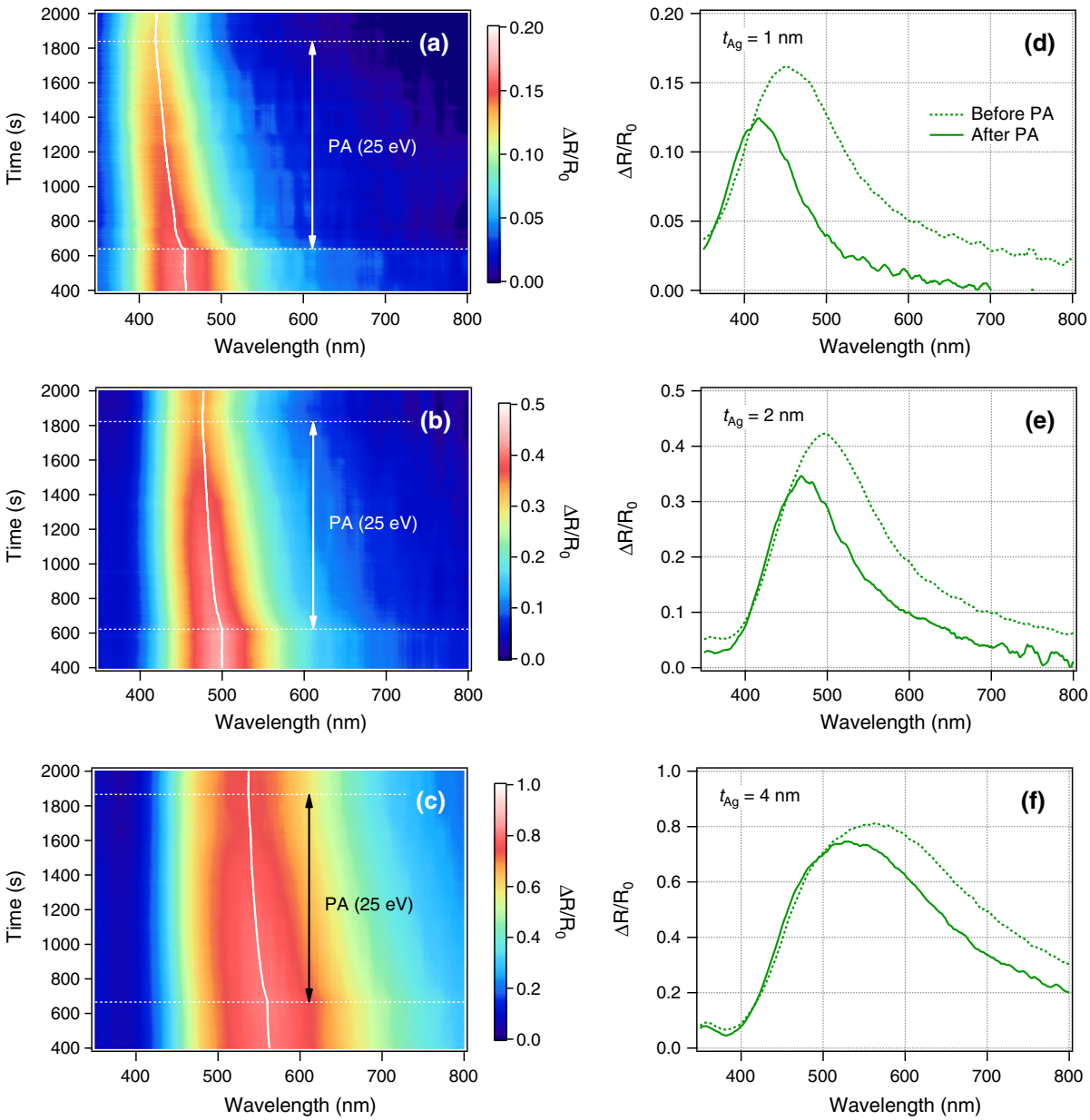

Fig. 7 SDRS signals $\Delta R/R_0(\lambda,t)$ collected during PA at 25 eV of Si_3N_4:Ag (t_{Ag}):Si_3N_4 nanocomposite thin films: **a** $t_{Ag} = 1$ nm, **b** $t_{Ag} = 2$ nm, and **c** $t_{Ag} = 4$ nm. The temporal variations of λ_{max} (i.e., spectral position of the maximum) are indicated by the *solid white lines*. SDRS signals $\Delta R/R_0(\lambda)$ collected before (*dotted lines*) and after (*solid lines*) PA treatment are also shown: **d** $t_{Ag} = 1$ nm, **e** $t_{Ag} = 2$ nm, and **f** $t_{Ag} = 4$ nm. Pay attention to the $\Delta R/R_0$ scale

be used to modify the structure of metal nanoclusters in a different way than treatments by traditional TA. Nevertheless, both TA and PA induce a prominent reshaping of the nanoclusters with an increase of their out-of-plane aspect ratio, which can strongly influence the optical response of the corresponding annealed nanocomposite thin films.

Influence of annealing treatments on the optical properties of Ag nanoclusters: ex situ reflectance measurements

Ex situ reflectance spectra collected for NA, TA-, and PA-treated Si_3N_4:Ag (2 nm):Si_3N_4 nanocomposite thin films are displayed in Fig. 6a–e. In Fig. 6a, a

maximum in the reflectance spectrum associated to the SPR of NA Ag nanoclusters embedded in the Si_3N_4 matrix is clearly observed at $\lambda_R \approx 645$ nm. As seen in Table 1, the SPR band peaks at a smaller (resp. larger) wavelength for $t_{Ag} = 1$ nm (resp. $t_{Ag} = 4$ nm), which can be ascribed to a larger (resp. smaller) *H*/*D* ratio for the nanoclusters. In comparison, for a given effective Ag thickness, the position of the maximum is significantly blue-shifted for nanoclusters subjected to annealing treatments (TA or PA). Actually, in qualitative agreement with the previous works reported in the literature (Takele et al. 2008; Pan et al. 2003; Heilmann and Werner 1998; Sancho-Parramon et al. 2010), TA at 400 °C induces a blue-shift of about 55 nm ($\lambda_R \approx 590$ nm) together with a narrowing of the SPR width, whereas the SPR amplitude is slightly increased (Fig. 6b). For PA-treated nanoclusters at 25 and 50 eV, blue-shifted SPRs of around 70 nm ($\lambda_R \approx 575$ nm) and 95 nm ($\lambda_R \approx 550$ nm) can be noticed in Fig. 6c, d, respectively. Besides, although a broad maximum around 400 nm is observed in the reflectance spectrum of Fig. 6e, the optical response of the nanocomposite thin film treated with PA at 80 eV is more likely due to interference effects generated from a cluster-free Si_3N_4 layer rather than a SPR from Ag nanoclusters (Simonot et al. 2010).

In order to confirm that the optical changes arise from structural modifications induced by annealing treatments of Ag nanoclusters, simulations of reflectance spectra were performed using an effective medium model assuming a three-layer structure Si_3N_4 (20 nm):Ag–Si_3N_4 (*H*):Si_3N_4 (40 nm) where the intermediate Ag–Si_3N_4 nanocomposite layer is considered as a homogeneous layer with thickness equal to the height *H* of the Ag nanoclusters. The dielectric functions of the glass substrate, Si_3N_4 layers, and metal nanoclusters have been obtained from spectroscopic ellipsometry measurements of pure materials (bulk or thin films). The effective dielectric function of the nanocomposite layer has been calculated assuming identical electrostatic dipoles with spheroidal shape (with the revolution axis normal to the substrate) and isotropic 2D distribution (Toudert et al. 2008; Camelio et al. 2009; Toudert et al. 2012). Figure 6f–i show reflectance spectra calculated for Si_3N_4:Ag (2 nm):Si_3N_4 nanocomposite thin films using the structural parameters collected in Table 1 as input parameters in the effective medium model. Overall, the experimental reflectance spectra are well

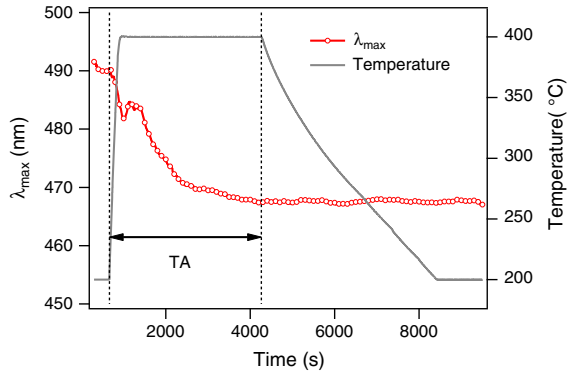

Fig. 8 Temporal variation of λ_{max} collected during TA at 400 °C of a Si_3N_4:Ag (2 nm):Si_3N_4 nanocomposite thin film. The corresponding variation of the temperature is also displayed

reproduced by the simulations (except the SPR width due to the monodisperse assumption), and particularly the relative spectral variations of the SPR position (i.e., compared to the NA sample, annealed samples display a blue-shifted SPR position). Moreover, as shown in Fig. 6j, the reflectance spectrum calculated by considering a single cluster-free Si_3N_4 layer (60 nm thick) is similar to the experimental reflectance spectrum of the Si_3N_4:Ag (2 nm):Si_3N_4 nanocomposite thin films treated with PA at 80 eV, which confirms that Ag was entirely sputtered during this PA treatment. On the whole, these results demonstrate that low-energy PA can be used as an effective method to modify the structure of metallic nanostructures and to tune their plasmonic properties accordingly.

Kinetics of annealing treatments: in situ and real-time SDRS measurements

Figure 7a–c show the real-time SDRS signals $\Delta R/R_0(\lambda,t)$ collected during PA at 25 eV of Si_3N_4:Ag (t_{Ag}):Si_3N_4 nanocomposite thin films with $t_{Ag} =$ 1 nm, 2 nm, and 4 nm, respectively. As mentioned before, the reflectance of the Si_3N_4 buffer-layer on glass is taken as reference $R_0(\lambda)$, and time $t = 0$ corresponds to the start of the Ag deposition. Nevertheless, in the following, the discussion is restricted to real-time optical variations arising during annealing treatments, which starts at $t \approx 650$ s and finishes at $t \approx 1{,}850$ s. In accordance with ex situ reflectance measurements of NA nanocomposite thin films collected after capping the nanoclusters with a Si_3N_4

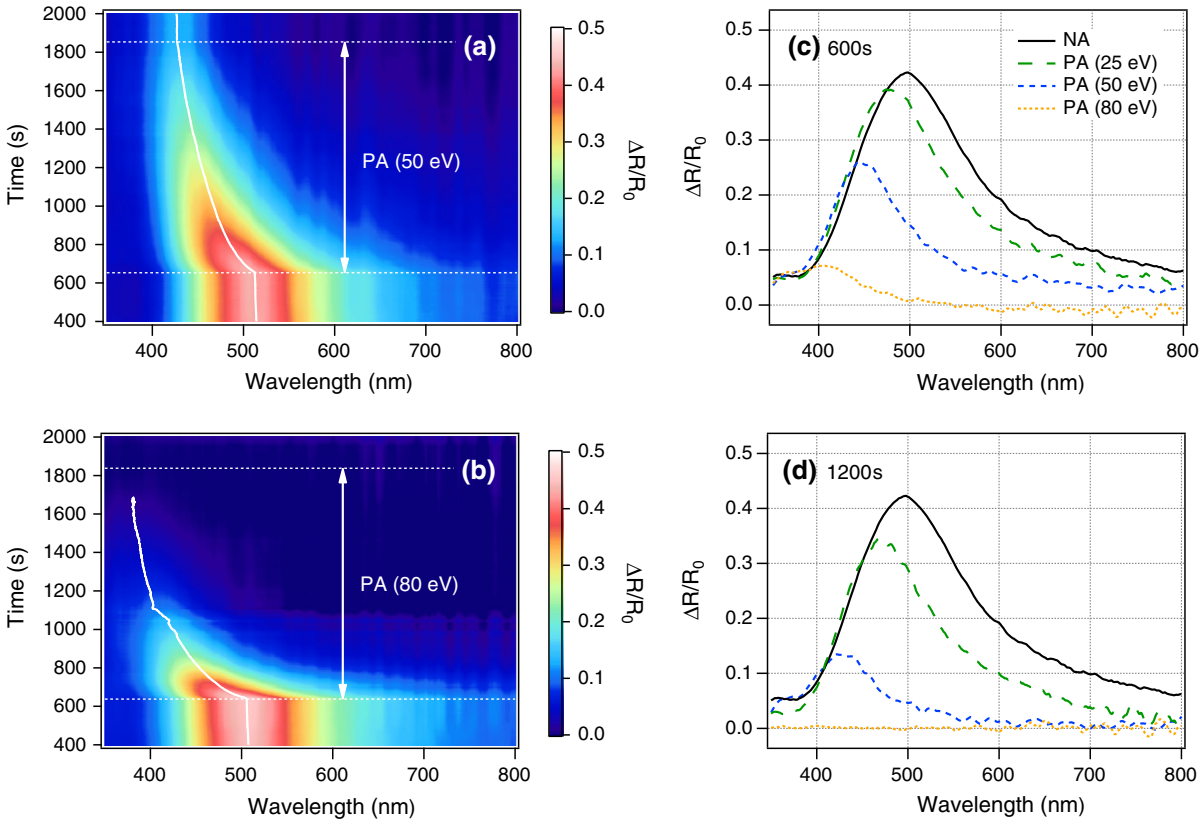

Fig. 9 SDRS signals $\Delta R/R_0(\lambda,t)$ collected during PA of Si_3N_4:Ag (2 nm):Si_3N_4 nanocomposite thin films: **a** at 50 eV and **b** at 80 eV. The temporal variations of λ_{max} are indicated by the *solid white lines*. SDRS signals $\Delta R/R_0(\lambda)$ collected after 600 s **c** and 1,200 s **d** of PA treatment at 25, 50, and 80 eV, respectively, are compared to a NA sample with similar Ag amount ($t_{Ag} = 2$ nm)

layer (Table 1), SDRS signals of Si_3N_4:Ag (t_{Ag}) samples before PA display a maximum at spectral position λ_{max} associated to the SPR of uncapped Ag nanoclusters, with λ_{max} being red-shifted when t_{Ag} is increased as a consequence of H/D decrease (see also Fig. 7d–f). Nevertheless, λ_{max} appears consistently smaller than λ_R (Table 1) because, among other reasons, the refractive index of the medium surrounding the nanoclusters is increased after Si_3N_4 capping (Simonot et al. 2010). Whatever the effective thickness of deposited Ag, t_{Ag}, PA at 25 eV causes an immediate blue-shift of the SPR, which gradually progresses with time and stops as soon as the bias plasma is switched off. These results show that the structural (and optical) modifications induced by low-energy PA are permanent and irreversible. As shown in Fig. 7d–f, in addition to the SPR blue-shift, PA at 25 eV also results in narrowing and decrease of the SPR, which can be associated to combined effects: decrease of the in-plane diameter of the nanoclusters, narrowing of the size distribution, increase of the out-of-plane ratio, and Ag re-evaporation by etching. Moreover, in agreement with postmortem structural analysis, modifications of the optical properties during PA at 25 eV are obviously more pronounced at smaller t_{Ag}, which suggests that small nanoclusters are more sensitive to PA effects than large nanoclusters.

It is worth noting that a progressive and irreversible blue-shift of the SPR is also observed in Fig. 8 during TA at 400 °C, although the kinetics of optical variations are different. While the kinetics of TA-induced modifications strongly depend on the annealing temperature, duration, and heating rate, PA offers flexibility via the control of the RF bias voltage. Effects of increasing the RF bias voltage on the SDRS signal of PA-treated Si_3N_4:Ag (2 nm):Si_3N_4 nanocomposite thin films are shown in Figs. 7b and 9a, b. During plasma annealing, whatever the bias voltage, a

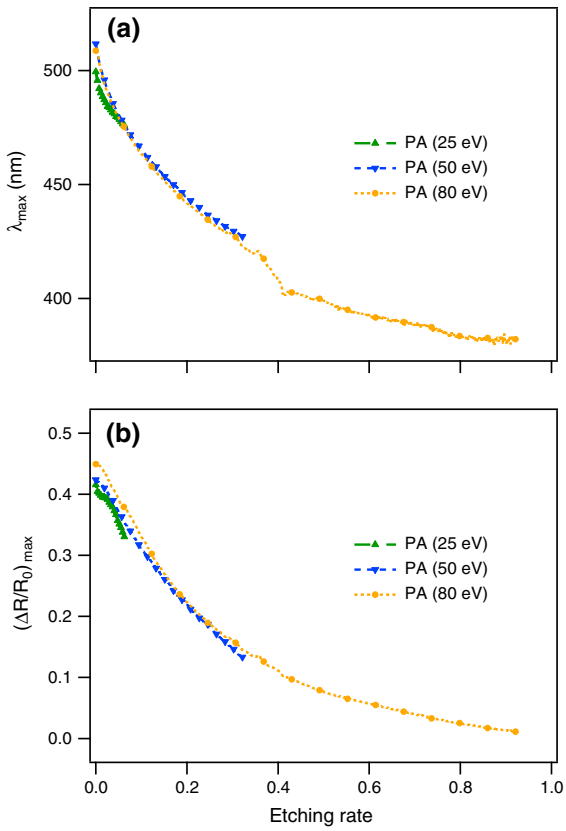

Fig. 10 Variations of **a** λ_{max} and **b** $(\Delta R/R_0)_{max}$ for PA-treated Si_3N_4:Ag (2 nm):Si_3N_4 nanocomposite thin films at 25, 50, and 80 eV. The time scale was converted into an etching rate scale, which results in superimposed curves for the three samples

prominent decrease in λ_{max} as well as a strong decrease of the SPR amplitude are evident. These effects are highlighted in Fig. 9c, d, which exhibit the SDRS signals of the PA-treated Si_3N_4:Ag (2 nm):Si_3N_4 nanocomposite thin films recorded after 600 and 1,200 s of treatment at 25, 50, and 80 eV, respectively, and compared to a NA sample with similar Ag amount. Our results clearly indicate that these optical modifications during PA are stronger for higher bias voltages. In other words, the increase of the bias voltage seems to fasten the optical changes. Accordingly, for the Si_3N_4:Ag (2 nm):Si_3N_4 nanocomposite thin films PA-treated at 80 eV, a complete disappearance of the SPR with $\Delta R/R_0 = 0$ at all wavelengths (due to total Ag re-evaporation by etching) is observed after about 1,050 s of PA. In Fig. 10, the variations of the spectral position λ_{max} and the corresponding SDRS amplitude, i.e., $(\Delta R/R_0)_{max} = \Delta R/R_0(\lambda_{max})$, are plotted versus a rescaled time scale for the PA-treated Si_3N_4:Ag (2 nm):Si_3N_4 nanocomposite thin films. Actually, the time scale was converted into an "etching rate" scale, which varies from 0 (corresponding to the start of the PA) to 1 (corresponding to 1,050 s of PA at 80 eV). It is worth noting that a fairly good superimposition of both λ_{max} and $(\Delta R/R_0)_{max}$ variations are obtained for the three samples by considering optical modifications 16.7 (resp. 3.2) times slower at 25 eV (resp. 50 eV) than at 80 eV. In other words, an "etching rate" of 5 % is obtained after 950 s at 25 eV, 185 s at 50 eV, and only 57 s at 80 eV. As discussed earlier, such changes in the SPR characteristics are the outcome of structural evolutions of Ag nanoclusters under PA, which induces, in particular, both a significant decrease of the in-plane diameter D of the nanoclusters and an increase of their out-of-plane ratio H/D. Our results tend to confirm that, in addition to enhanced Ag mobility, etching effects also contribute importantly to the morphological evolution of the nanoclusters subjected to low-energy ion species, even at 25 eV. As a result, the control of the RF bias voltage during PA treatment of plasmonic nanostructures gives an interesting flexibility to tune the rate of morphological changes, and therefore, the rate of optical modifications.

Conclusion

In this article, the influence of TA and low-energy plasma annealing on the structural and optical properties of Ag nanoclusters with sizes between 2 and 25 nm has been studied by combining postmortem characterizations (HAADF-STEM, GISAXS, and reflectance measurements) and real-time SDRS. Both TA and PA treatments induce a progressive and irreversible reshaping of the nanoclusters with an increase of their out-of-plane aspect ratio, which accordingly causes a prominent blue-shift of the associated SPR. However, whereas TA leads to a decrease of the areal cluster density due to atomic or cluster migration and coalescence, low-energy PA produces a significant decrease of both the cluster size and intercluster distance. Moreover, the structural and optical modifications are found to be more pronounced when decreasing the nanocluster size and increasing the RF bias voltage, ultimately resulting in total Ag re-evaporation. These results highlight the important

contribution of etching and re-deposition effects during PA, which appears as an efficient post-deposition method to modify the morphology of nanoclusters and to tune their physical properties. The kinetics of the optical modifications has been investigated in real-time thanks to in situ SDRS measurements, thus demonstrating that the strength of the PA treatment on Ag nanoclusters can be easily controlled by varying the RF bias voltage and the treatment duration. Accordingly, optimization of such low-temperature plasma treatments could offer additional potential for generating functional nanostructures with tailored properties and predictible performances.

Acknowledgments Authors acknowledge the assistance from staff at the D2AM beamline (ESRF, Grenoble) during GISAXS experiments. They also thank Ph. Guérin and F. Pailloux for important contributions in sample fabrication by magnetron sputtering and structural characterization by HAADF-STEM, respectively. Author VA is grateful to "Région Poitou–Charentes" for providing the financial support for this research project.

References

Antad V, Simonot L, Babonneau D, Camelio S, Pailloux F, Guérin P (2012) Monitoring the reactivity of Ag nanoparticles in oxygen atmosphere by using in situ and real-time optical spectroscopy. J Nanophotonics 6:061502

Antad V, Simonot L, Babonneau D (2013) Tuning the surface plasmon resonance of silver nanoclusters by oxygen exposure and low-energy plasma annealing. Nanotechnology 24:045606

Babonneau D (2010) FITGISAXS: software package for modelling and analysis of gisaxs data using igor pro. J Appl Crystallogr 43:929–936

Bedel L, Cayron C, Jouve M, Maury F (2012) Embedded layer of Ag nanoparticles prepared by a combined PECVD/PVD process producing Sio_xC_y–Ag nanocomposite thin films. Nanotechnology 23:015603

Bhattacharyya SR, Datta D, Shyjumon I, Smirnov BM, Chini TK, Ghose D, Hippler R (2009) Growth and melting of silicon supported silver nanocluster films. J Phys D 42:1–9

Bi H, Cai W, Kan C, Zhang L, Martin D, Träger F (2002) Optical study of redox process of Ag nanoparticles at high temperature. J Appl Phys 92:7491–7497

Borensztein Y, Delannoy L, Djedidi A, Barrera RG, Louis C (2010) Monitoring of the plasmon resonance of gold nanoparticles in Au/Tio_2 catalyst under oxidative and reducing atmospheres. J Phys Chem C 114:9008–9021

Camelio S, Babonneau D, Lantiat D, Simonot L, Pailloux F (2009) Anisotropic optical properties of silver nanoparticle arrays on rippled dielectric surfaces produced by low-energy ion erosion. Phys Rev B 80:155434

Chey SJ, Cahill DG (1997) Surface defects created by low energy ($20 < E < 240$ eV) ion bombardment of Ge(001). Surf Sci 380:377–384

Dong ZW, You GJ, Zhou P, Zhang CF, Liu KJ, Yan YL, Qian SX (2006) Heat treatment effect on the ultrafast dynamics and nonlinear optical properties of $Ag:Si_3n_4$ nanocermets. J Phys D 39:4766–4770

Esch S, Bott M, Michely T, Comsa G (1995) Nucleation of homoepitaxial films grown with ion assistance on Pt(111). Appl Phys Lett 67:3209–3211

Heilmann A, Werner J (1998) In situ observation of microstructural changes of embedded silver particles. Thin Solid Films 317:21–26

Henry C (2005) Morphology of supported nanoparticles. Prog Surf Sci 80:92–116

Hu J, Cai W, Li Y, Zeng H (2005) Oxygen-induced enhancement of surface plasmon resonance of silver nanoparticles for silver-coated soda-lime glass. J Phys 17:5349

Iline A, Simon M, Stietz F, Träger F (1999) Adsorption of molecules on the surface of small metal particles studied by optical spectroscopy. Surf Sci 436:51–62

Kinnan MK, Chumanov G (2010) Plasmon coupling in two-dimensional arrays of silver nanoparticles: II. Effect of the particle size and interparticle distance. J Phys Chem C 114:7496–7501

Kolmakov A, Goodman DW (2002) In situ scanning tunneling microscopy of oxide-supported metal clusters: nucleation, growth, and thermal evolution of individual particles. Chem Rec 2:446–457

Kreibig U, Vollmer M (1995) Optical properties of metal clusters. Springer, Berlin

Lantiat D, Babonneau D, Camelio S, Pailloux F, Denanot MF (2007) Evidence for capping-layer effects on the morphology and plasmon excitation of Ag nanoparticles. J Appl Phys 102:113518

Lapsley MI, Shahravan A, Hao Q, Juluri BK, Giardinelli S, Zhao Y, Lu M, Chiang IK, Matsoukas T, Huang TJ (2012) Shifts in plasmon resonance due to charging of a nanodisk array in argon plasma. Appl Phys Lett 100:101903

Maier SA, Atwater HA (2005) Plasmonics: localization and guiding of electromagnetic energy in metal/dielectric structures. J Appl Phys 98:011101

Mock JJ, Barbic M, Smith DR, Schultz DA, Schultz S (2002) Shape effects in plasmon resonance of individual colloidal silver nanoparticles. J Chem Phys 116:6755–6759

Pan A, Yang Z, Zheng H, Liu F, Zhu Y, Su X, Ding Z (2003) Changeable position of SPR peak of Ag nanoparticles embedded in mesoporous Sio_2 glass by annealing treatment. Appl Surf Sci 205:323–328

Polman A (2008) Plasmonics. Science 322:868–869

Ren M, Jia B, Ou JY, Plum E, Zhang J, MacDonald KF, Nikolaenko AE, Xu J, Gu M, Zheludev NI (2011) Nanostructured plasmonic medium for terahertz bandwidth all-optical switching. Adv Mater 23:5540–5544

Ruffino F, Grimaldi MG, Bongiorno C, Giannazzo F, Roccaforte F, Raineri V (2008) Microstructure of Au nanoclusters formed in and on SiO_2. Superlatt Microstruct 44:588–598

Sancho-Parramon J, Janicki V, Dubček P, Karlušić M, Gracin D, Jakšić M, Bernstorff S, Meljanac D, Juraić K (2010) Optical and structural properties of silver nanoparticles in

glass matrix formed by thermal annealing of field assisted film dissolution. Opt Mater 32:510–514

Schuller JA, Barnard ES, Cai W, Jun YC, White JS, Brongersma ML (2010) Plasmonics for extreme light concentration and manipulation. Nature Mater 9:193–204

Serna R, Babonneau D, Suárez-García A, Afonso CN, Fonda E, Traverse A, Naudon A, Hole DE (2002) Effect of oxygen pressure on the optical and structural properties of $Cu:Al_2O_3$ nanocomposite films. Phys Rev B 66:205402

Simonot L, Babonneau D, Camelio S, Lantiat D, Guérin P, Lamongie B, Antad V (2010) In situ optical spectroscopy during deposition of $Ag:Si_3N_4$ nanocomposite films by magnetron sputtering. Thin Solid Films 518:2637–2643

Takele H, Kulkarni A, Jebril S, Chakravadhanula VSK, Hanisch C, Strunskus T, Zaporojtchenko V, Faupel F (2008) Plasmonic properties of vapour-deposited polymer composites containing Ag nanoparticles and their changes upon annealing. J Phys D 41:125409

Tang J, Photopoulos P, Tserepi A, Tsoukalas D (2011) Two-dimensional nanoparticle self-assembly using plasma-induced Ostwald ripening. Nanotechnology 22:235306

Teranishi T, Tasegawa S, Shimizu T, Miyake M (2001) Heat-induced size evolution of gold nanoparticles in the solid state. Adv Mater 13:1699–1701

Toudert J, Camelio S, Babonneau D, Denanot MF, Girardeau T, Espiños JP, Yubero F, Gonzalez-Elipe AR (2005) Morphology and surface-plasmon resonance of silver nanoparticles sandwiched between Si_3N_4 and BN layers. J Appl Phys 98:114316

Toudert J, Babonneau D, Simonot L, Camelio S, Girardeau T (2008) Quantitative modelling of the surface plasmon resonances of metal nanoclusters sandwiched between dielectric layers: the influence of nanocluster size, shape and organization. Nanotechnology 19:125709

Toudert J, Simonot L, Camelio S, Babonneau D (2012) Advanced optical effective medium modeling for a single layer of polydisperse ellipsoidal nanoparticles embedded in a homogeneous dielectric medium: surface plasmon resonances. Phys Rev B 86:045415